Geochemical Perspectives Letters

Imaging of boron in altered mantle rocks illuminates progressive serpentinisation episodes

A.D. Evans, C.D. Standish, J.A. Milton, A.G. Robinson, D. Craw, G.L. Foster, D.A.H. Teagle

Supplementary Information

The Supplementary Information includes:

- Analytical Methods
- References for Figures 3 and 4
- Tables S-1 to S-4
- Figure S-1
- Supplementary Information References

Analytical Methods

All samples were prepared and analysed at the School of Ocean and Earth Science Geochemistry Research Facility, National Oceanography Centre Southampton (NOCS), University of Southampton. Samples were sawn to remove surficial weathering rinds and ground to remove contamination from the saw blade. Polished thick sections were prepared to a thickness of ~300 µm. Samples designated for grinding were then washed and ultra-sonicated in Milli-Q (18.2 MΩ H_2O) water and left to dry overnight in an oven at 65 °C. After drying, rock samples were crushed using a manual iron fly-press and wrapped in paper between plastic chopping boards to avoid trace metal contamination. Rock samples were then powdered using a chrome-steel jar mill in a Rocklabs grinder. Prior to analysis, powdered rock samples and standards UB-N and BCR-2 were pressed into pellets using a manual hydraulic press under a pressure equivalent to a mass of 10 T over a period of 30 minutes. An additional standard reference glass BCR-2g was mounted in epoxy resin and polished. Boron concentrations of pressed powder pellets (PPP) and in situ boron concentrations and boron isotopic compositions of thick sections were determined using an Elemental Scientific Lasers NWR193 Excimer laser ablation (LA) system with a TwoVol2 ablation cell (Bozeman, MT, USA). Prior to the acquisition of data, samples

and standards were pre-ablated at reduced power (20 %), lower repetition rate (10 Hz), and a faster raster ablation mode (200 µm/s) to remove any contaminants from the surface of the prepared polished thick section or pressed powder pellet.

Boron isotope analyses of polished thick sections were acquired using a Thermo Scientific (Thermo Fisher Scientific, Waltham, MA, USA) Neptune Plus multi-collector inductively coupled plasma (MC-ICP) mass spectrometer equipped with Faraday cup detectors, where ^{10}B and ^{11}B intensities were measured on the L3 and H3 Faraday cups, respectively. Tuning protocols for the LA-MC-ICP-MS method were optimised for sensitivity and stability, broadly following the procedure detailed in (Standish *et al.*, 2019). Typical operating parameters for the laser ablation system were a beam area of 50 x 150 µm, laser power at 50 % (yielding ~6.7 J/cm^2), repetition rate of 50 Hz, raster ablation mode tracking at 10 µm/s . Acquisition of reference materials and samples typically integrate ~100 cycles, manifest as a ~1 mm track on the surface of the thick sections. Samples were run with a forward and backward ablation, resulting in a total ~2 mm ablated distance. Gas flow rates during analyses were typically: 750 mL/minute for He, 17 mL/minute for N, and 1.035 mL/minute for Ar. A 40 second on-peak gas blank was analysed before and after ablation, with 60 seconds allowed for sample wash-out prior to the latter. Dynamic blank corrections were applied cycle by cycle assuming a linear relationship between the preceding and succeeding blank measurements. Instrumental mass bias was corrected by sample-standard bracketing with USGS glass reference material BCR-2g and using the reference value $^{11}B/^{10}B$ of 4.035, $\delta^{11}B$ -3.83 ‰ (Kimura *et al.*, 2016). Typically, two analyses of BCR-2g would bracket an analysis of reference serpentinite UB-N pellet with <20 minutes ablation time between analyses of BCR-2g. Data were evaluated offline with cycles falling outside of 3σ of the mean removed. Integration time of the instrument was set to ~2 seconds per cycle. Precision and accuracy of the methodology was assessed using similarly analysed pressed powder pellets of reference materials UB-N and BCR-2. The mean internal precision (2 standard errors (SE)) of UB-N and BCR-2 pellets were ± 0.6 ‰ and ± 1.3 ‰ respectively. The mean $\delta^{11}B$ values of UB-N and BCR-2 were +13.5 ± 2.0 ‰ (2σ, n=20) and -5.5 ± 2.2 ‰ (2σ, n=12), resulting in mean inaccuracies in $\Delta\delta^{11}B$, defined as $\delta^{11}B_{Reported}$ - $\delta^{11}B_{Laser}$ following (Standish *et al.*, 2019) of 0.4 ‰ for UB-N and -0.4 ‰ for BCR-2 (**Table S-1**).

Boron concentration maps of polished thick sections were analysed with the laser ablation system coupled to an Agilent (Agilent Technologies Inc., CA, USA) 8900 Triple Quadrupole ICP-MS. Typical operating parameters for the laser ablation system were a beam area of 10 x 10 µm, repetition rate of 50 Hz, raster ablation mode tracking of 20 µm/s, and a laser power density of ~6 J/cm^2. The Agilent ICP-MS acquisition time was ~0.375 seconds per cycle. Gas flow rates during analyses were typically: 800 mL/minute for He, 4 mL/minute for N, and 0.6 mL/minute for Ar. The area mapped was 3336 x 3000 µm, requiring ~18 hours of instrument acquisition time.

Spot boron concentrations of polished thick sections and pressed powder pellets were determined using the laser ablation system coupled to a Thermo Scientific Element 2 ICP-MS. Typical operating parameters for the laser ablation system were a beam area of 50 x 150 µm, repetition rate of 30 Hz, raster ablation mode tracking of 10 µm/s, and a laser power density of ~6 J/cm^2. The integration time was 2 seconds per cycle. Gas flow rates during analyses were typically: 800 mL/minute for He, 4 mL/minute for N, and 0.6 mL/minute for Ar. Data was evaluated offline with both dynamic

blank and drift correction. The mean internal precision (2 SE) of the reference materials UB-N and BCR-2g for boron concentration determination were ± 4.4 µg/g and ± 0.4 µg/g respectively. The mean determined B concentrations of UB-N and BCR-2g were 136.4 ± 8.4 µg/g (2σ, n=80) and 2.7 ± 1.2 µg/g (2σ, n=80) respectively, resulting in mean inaccuracies (ΔB, defined as $B_{Reported}$ - B_{Laser}) of 3.6 µg/g for UB-N and 5.3 µg/g for BCR-2g (**Table S-1**).

Analytical results are reported in Table S-1, Table S-2, and Table S-3.

References for Figures 3 and 4

On Figure 3 the boundaries of B (µg/g) and $\delta^{11}B$ for Troodos volcanic glasses are from Fonseca *et al.*, (2017), modern seawater Foster *et al.*, (2010) and Spivack and Edmond (1987), Messinian evaporites Paris *et al.*, (2010) and primitive mantle Chaussidon and Jambon (1994). Cyprus meteoric water concentration are from Rose-Koga *et al.* (2006), meteoric water boron isotope composition is estimated from the equations of Boronina *et al.*, (2005) and Rose-Koga *et al.* (2006).

On Figure 4 the compiled serpentinite values are from the: Mariana forearc (Benton *et al.*, 2001); Mid-ocean ridge serpentinite, Atlantis Massif (Boschi *et al.*, 2008), Mid-Atlantic Ridge ODP Leg 209 (Vils *et al.*, 2009), and dredged serpentinites (Spivack and Edmond, 1987); 'Ophiolitic' serpentinite, Cerro Del Almirez (Harvey *et al.*, 2014), ophiolitic serpentinites (Martin *et al.*, 2016), Corsica and Western Alps (Martin *et al.*, 2020), Californian serpentinites (Yamada *et al.*, 2019), and Erro Tobbio serpentinite (Scambelluri and Tonarini, 2012). Boundaries of B (µg/g) and $\delta^{11}B$ of Troodos volcanic glasses (Fonseca *et al.*, 2017), modern seawater (Foster *et al.*, 2010; Spivack and Edmond, 1987), and primitive mantle (Chaussidon and Jambon, 1994; Marschall *et al.*, 2017) are also shown.

Supplementary Tables

Table S-1 $\delta^{11}B$ Precision and accuracy table for LA-MC-ICP-MS and LA-ICP-MS

	$\delta^{11}B$ (‰) Reference Value	$\delta^{11}B$ (‰) This study	$\Delta\delta^{11}B$	B (µg/g) Reference Value	B (µg/g) This study	ΔB
UB-N (pressed powder pellet)	+13.1 ‰ (Gangjian et al., 2013)	+13.5 ± 2 ‰ (2σ, n=20)	+0.4 ‰	140 µg/g (Govindaraju, 1995)	136.4 ± 8.4 µg/g (2σ, n=80)	3.6 µg/g
BCR-2 (pressed powder pellet)	-5.9 ‰ (Gangjian *et al.*, 2013)	-5.5 ± 2.2 ‰ (2σ, n=12)	-0.4 ‰	4.3 ± 3.9 µg/g (2σ; n=7; compiled (Jochum *et al.*, 2005)	-	-
BCR-2g (glass)	-3.8 ‰ (Kimura *et al.*, 2016)	-	-	8 ± 8.1 µg/g (2σ; n=34; compiled Jochum *et al.*, 2005)	2.7 ± 1.2 µg/g (2σ, n=80)	5.3 µg/g

Table S-2 In situ polished thick section summary results

	Mesh Texture		Serpentine Vein		Chrysotile Vein		All in situ polished thick sections		Whole Rock	Serpentine Vein	Chrysotile Vein	All Pressed Powder Pellets
	$\delta^{11}B$ (‰)	B (ug/g)	$\delta^{11}B$ (‰)	B (ug/g)	$\delta^{11}B$ (‰)	B (ug/g)	$\delta^{11}B$ (‰)	B (ug/g)	B (ug/g)	B (ug/g)	B (ug/g)	B (ug/g)
# of samples	26	26	20	20	3	3	49	49	17	6	2	25
Average	11.5	26	12	12	15.3	35	11.9	21	34	6	12	25
1σ (symmetric)	2.7	12	3.9	11	1.1	7	3.2	13	21	3	3	21
Median	11.5	25	11.9	9	15.1	35	11.9	19	29	4	12	24
1σ (asymmetric)	+2.3/-2.9	+11/-13	+4.1/-3.7	+8/-6	+1/-0.5	+5/-5	+3.6/-3.6	+16/-12	+21/-15	+6/-1	+1/-1	+15/-17
Min	5.8	7	6.9	3	14.3	28	5.8	3	7	3	10	3
Max	16.2	49	18.4	47	16.5	42	18.4	49	80	10	14	80

Table S-3 (overleaf) In situ boron concentrations and boron isotopic compositions of polished thick sections.

Table S-3 Sample Name	Sample Type	Sample Area	$^{11}B/^{10}B$	±2SE	δ11B	±2SE	B (µg/g)	±2SE
AA4-1	Mesh texture	Artemis	4.0776	0.0028	6.72	0.70	11.30	0.34
AA4-3	Mesh texture	Artemis	4.0807	0.0032	7.49	0.79	27.60	0.67
AA4-5	Serpentine Vein	Artemis	4.0835	0.0058	8.18	1.41	4.65	0.67
AA4-7	Serpentine Vein	Artemis	4.0790	0.0038	7.08	0.94	3.05	0.09
AA4-9	Serpentine Vein	Artemis	4.0833	0.0039	8.15	0.95	3.82	0.23
AA4-11	Serpentine Vein	Artemis	4.0886	0.0036	9.46	0.89	3.97	0.07
AH1-3 2	Mesh texture	Olympus	4.0851	0.0035	8.58	0.86	36.23	0.69
AH1-3 4	Mesh texture	Olympus	4.0845	0.0043	8.43	1.04	29.00	1.37
AH1-3 5	Mesh texture	Olympus	4.0853	0.0053	8.63	1.29	20.41	0.63
AR3-1 conc line	Mesh texture	Artemis	4.1068	0.0008	13.97	0.19	35.27	0.58
AR3-1 serp andradite	Serpentine andradite Vein	Artemis	4.1000	0.0007	12.27	0.18	33.96	0.35
AR3-1 chrysotile	Chrysotile Vein	Artemis	4.1170	0.0009	16.50	0.22	34.86	0.52
AR3-1 recrystallised	Mesh texture	Artemis	4.1034	0.0016	13.11	0.40	41.75	1.48
AR3-1 lower chrysotile	Chrysotile Vein	Artemis	4.1114	0.0015	15.09	0.37	28.07	1.70
AR3-1 Ribbon	Mesh texture	Artemis	4.1040	0.0040	13.27	0.99	46.24	1.81

Table S-3 Sample Name	Sample Type	Sample Area	$^{11}B/^{10}B$	±2SE	δ11B	±2SE	B (µg/g)	±2SE
AR3-1 Serpentine in centre	Serpentine Vein	Artemis	4.1067	0.0054	13.95	1.32	48.65	0.47
AH2-1 1	Mesh texture	Olympus	4.0936	0.0063	10.69	1.53	11.87	0.49
AH2-1 6	Black fine grained serpentine vein	Olympus	4.1074	0.0058	14.11	1.40	6.28	0.98
AH2-1 black vein	Black fine grained serpentine vein	Olympus	4.0879	0.0019	9.28	0.47	10.58	0.44
AH2-1 2	Mesh texture	Olympus	4.1049	0.0022	13.51	0.53	12.52	0.70
AH2-1 3	Mesh texture	Olympus	4.1160	0.0021	16.24	0.52	13.08	0.60
AH2-1 4	Mesh texture	Olympus	4.1024	0.0015	12.88	0.38	13.08	1.61
BA1-X1	Mesh texture	Artemis	4.0957	0.0023	11.22	0.56	23.70	0.56
BA1-X2	Mesh texture	Artemis	4.0943	0.0019	10.87	0.47	22.41	0.75
BA1 X3	Mesh texture	Artemis	4.1131	0.0027	15.52	0.65	28.88	2.00
BA1 X4	Serpentine Vein	Artemis	4.1160	0.0027	16.24	0.67	13.22	1.59
BA1 X5	Serpentine Vein	Artemis	4.1204	0.0031	17.33	0.76	3.83	0.20
BA1 X6	Serpentine Vein	Artemis	4.1248	0.0040	18.41	0.98	3.78	0.17
BA1 Y1	Mesh texture	Artemis	4.1033	0.0046	13.09	1.12	20.66	1.92

Table S-3 Sample Name	Sample Type	Sample Area	$^{11}B/^{10}B$	±2SE	δ11B	±2SE	B (µg/g)	±2SE
BA1 Y2	Serpentine Vein	Artemis	4.1095	0.0042	14.64	1.01	6.61	0.50
BA1 Y3	Serpentine Vein	Artemis	4.1147	0.0028	15.93	0.68	13.57	0.65
BA1 Y4	Black serpentine vein	Artemis	4.1150	0.0030	16.01	0.73	46.98	1.92
BA1 Y5	Mesh texture	Artemis	4.1139	0.0031	15.72	0.75	25.44	0.66
BA1 Z1	Serpentine Vein	Artemis	4.0981	0.0025	11.80	0.61	10.60	0.91
BA1 Z2	Serpentine Vein	Artemis	4.0987	0.0027	11.95	0.67	8.21	0.44
BA1 Z3	Serpentine Vein	Artemis	4.1024	0.0030	12.87	0.72	22.27	0.94
AX1 X1 mesh	Mesh texture	Artemis	4.0993	0.0010	12.10	0.25	18.36	0.34
AX1 X2 mesh	Mesh texture	Artemis	4.0974	0.0009	11.63	0.22	30.18	0.57
AX1 X3 recryz	Mesh texture	Artemis	4.0961	0.0013	11.32	0.32	33.33	0.40
AX1 X4 bastite	Mesh texture	Artemis	4.0900	0.0020	9.80	0.49	33.92	0.63
AX1 X5 vein edge	Mesh texture	Artemis	4.0970	0.0011	11.54	0.26	7.20	0.40
AX1 X6 polyg vein	Serpentine Vein	Artemis	4.0917	0.0009	10.22	0.22	17.80	0.59
AX1 X7 recryz vein ed	Mesh texture	Artemis	4.0966	0.0012	11.44	0.30	9.02	0.22
AX1 X8 recryz	Mesh texture	Artemis	4.0970	0.0013	11.54	0.31	34.71	0.84
AX1 X9 mesh	Mesh texture	Artemis	4.1017	0.0013	12.69	0.31	38.97	0.49

Table S-3 Sample Name	Sample Type	Sample Area	$^{11}B/^{10}B$	±2SE	δ11B	±2SE	B (µg/g)	±2SE
AX1 X10 chrysotile	Chrysotile Vein	Artemis	4.1082	0.0010	14.30	0.25	41.68	0.76
AJ1 Ant Back 1	Antigorite Vein	Olympus	4.0783	0.0006	6.91	0.14	9.80	0.18
AJ1 Ant Back 2	Antigorite Vein	Olympus	4.0782	0.0006	6.89	0.15	9.67	0.13

Table S-4 Pressed Powder Pellets Results Table

Sample	Location	Sample Type	B (µg/g)	±2SE
AG2	Olympus	Olympus Bulk Rock	58.18	2.25
AH1	Olympus	Olympus Bulk Rock	36.23	0.69
AH2	Olympus	Olympus Bulk Rock	11.24	2.12
CX1	Olympus	Olympus Bulk Rock	6.83	0.48
PP2	Olympus	Olympus Bulk Rock	26.29	0.52
CJ1	Olympus	Olympus Bulk Rock	10.23	0.49
AJ1	Olympus	Serpentine (antigorite) vein	9.80	0.18
CO1B	Olympus	Serpentine vein	2.50	0.55
CO2	Olympus	Serpentine vein	2.91	0.59
AA3	Artemis	Serpentine vein	3.05	0.09
BA1A	Artemis	Serpentine vein	3.78	0.17
CU5	Artemis	Serpentine vein	3.49	0.36
CR1	Artemis	Chrysotile	10.07	2.11
CU3	Artemis	Chrysotile vein	13.87	0.86
AA4-2	Artemis	Artemis Bulk Rock (Halo)	27.60	0.67
AO3C	Artemis	Artemis Bulk Rock (Halo)	35.26	1.42
BA1B	Artemis	Artemis Bulk Rock (Halo)	28.88	2.00
CU4	Artemis	Artemis Bulk Rock	25.89	2.32
CU2	Artemis	Artemis Bulk Rock	43.11	2.82
BA1C	Artemis	Artemis Bulk Rock	23.70	0.56
AO2	Artemis	Artemis Bulk Rock	75.77	10.36
AR1	Artemis	Artemis Bulk Rock	30.48	1.71
CU1	Artemis	Artemis Bulk Rock	38.37	4.45
AR2	Artemis	Artemis Bulk Rock	79.54	6.35
PP1	Artemis	Artemis Bulk Rock	16.68	0.65

Supplementary Figures

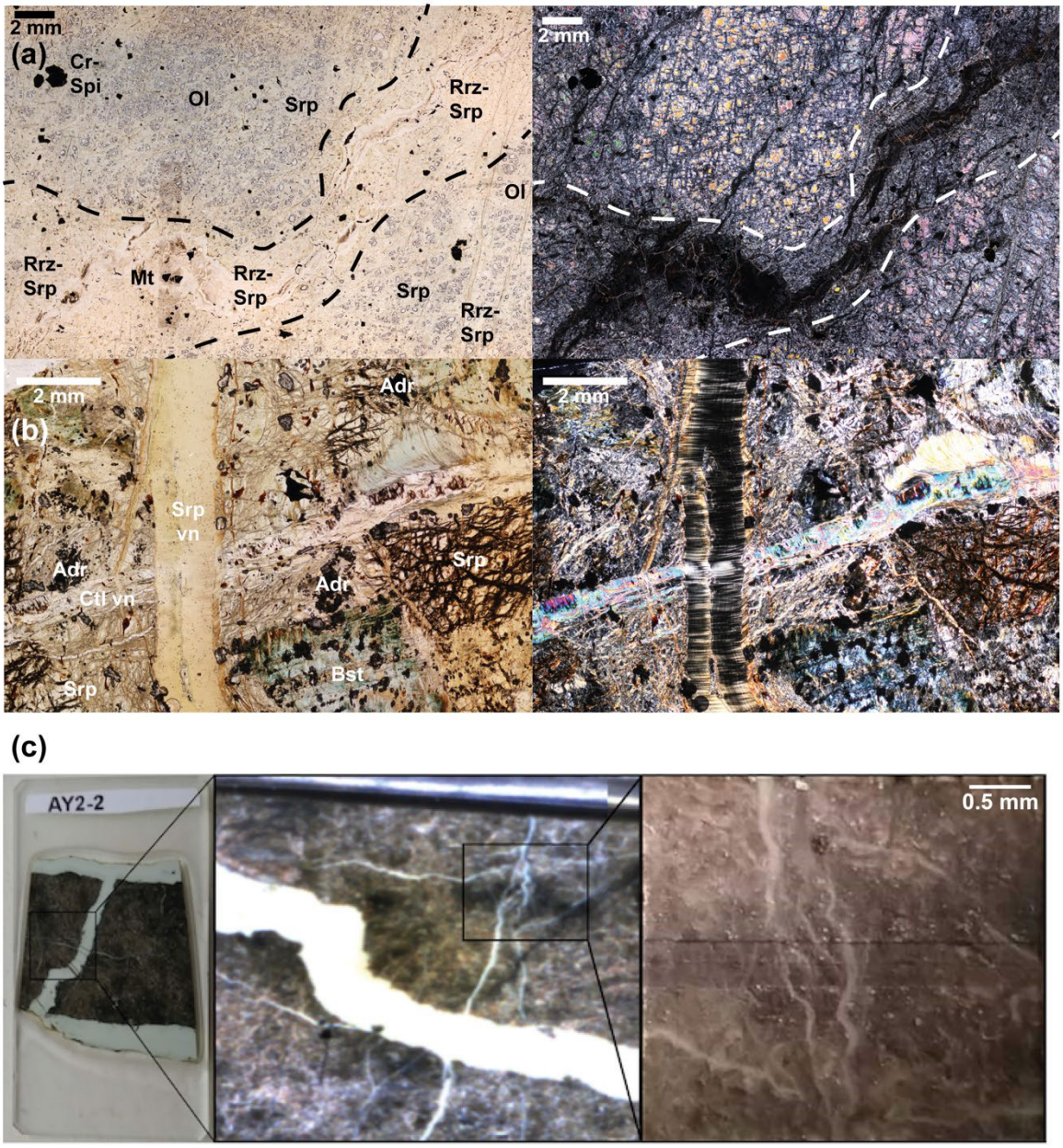

Figure S-1 (a) Representative sample of partially serpentinised mantle peridotite with olivine-serpentine mesh-texture and variably recrystallised irregular veins shown. Sample AH2 from the Olympus Diapir. **(b)** Representative sample of completely serpentinised mantle peridotite with a variably recrystallised mesh texture, crack-seal serpentine vein and fibrous chrysotile vein. Sample AX1 from the Artemis Diapir. Adr = Andradite, Srp vn = Serpentine vein, Ctl vn = Chrysotile vein, Bst = bastite (relict Opx), Ol = Olivine, Rrz-Srp = Recrystallised serpentine, Srp = Serpentine, Mt = Magnetite. **(c)** Image of thick section AY2-2 used for elemental mapping with magnified images of the mapped region.

Supplementary Information References

Benton, L.D., Ryan, J.G., Tera, F. (2001) Boron isotope systematics of slab fluids as inferred from a serpentine seamount, Mariana forearc. *Earth and Planetary Science Letters* 187, 273–282. https://doi.org/10.1016/S0012-821X(01)00286-2

Boronina, A., Balderer, W., Renard, P., Stichler, W. (2005) Study of stable isotopes in the Kouris catchment (Cyprus) for the description of the regional groundwater flow. *Journal of Hydrology* 308, 214–226. https://doi.org/10.1016/j.jhydrol.2004.11.001

Boschi, C., Dini, A., Früh-Green, G.L., Kelley, D.S. (2008) Isotopic and element exchange during serpentinization and metasomatism at the Atlantis Massif (MAR 30°N): Insights from B and Sr isotope data. *Geochimica et Cosmochimica Acta* 72, 1801–1823. https://doi.org/10.1016/j.gca.2008.01.013

Chaussidon, M., Jambon, A. (1994) Boron content and isotopic composition of oceanic basalts: Geochemical and cosmochemical implications. *Earth and Planetary Science Letters* 121, 277–291. https://doi.org/10.1016/0012-821X(94)90073-6

Fonseca, R.O.C., Kirchenbaur, M., Ballhaus, C., Münker, C., Zirner, A., Gerdes, A., Heuser, A., Botcharnikov, R., Lenting, C. (2017) Fingerprinting fluid sources in Troodos ophiolite complex orbicular glasses using high spatial resolution isotope and trace element geochemistry. *Geochimica et Cosmochimica Acta* 200, 145–166. https://doi.org/10.1016/j.gca.2016.12.012

Foster, G.L., Pogge von Strandmann, P.A.E., Rae, J.W.B. (2010) Boron and magnesium isotopic composition of seawater. *Geochemistry, Geophysics, Geosystems* 11(8). https://doi.org/10.1029/2010GC003201

Gangjian, W., Jingxian, W., Ying, L., Ting, K., Zhongyuan, R., Jinlong, M., Yigang, X. (2013) Measurement on high-precision boron isotope of silicate materials by a single column purification method and MC-ICP-MS. *Journal of Analytical Atomic Spectrometry* 28, 606–612. https://doi.org/10.1039/c3ja30333k

Govindaraju, K. (1995) 1995 working values with confidence limits for twenty-six CRPG, ANRT and IWG-GIT geostandards. *Geostandards Newsletter: The Journal of Geostandards and Geoanalysis* 19, 1-32. https://doi.org/10.1111/j.1751-908X.1995.tb00164.x

Harvey, J., Garrido, C.J., Savov, I., Agostini, S., Padrón-Navarta, A., Marchesi, C., López Sánchez-Vizcaíno, V., Gómez-Pugnaire, M.T. (2014) 11B-rich fluids in subduction zones: The role of antigorite dehydration in subducting slabs and boron isotope heterogeneity in the mantle. *Chemical Geology* 376, 20–30. https://doi.org/10.1016/j.chemgeo.2014.03.015

Jochum, K.P., Nohl, U., Herwig, K. (2005) GeoReM: a new geochemical database for reference materials and isotopic standards. *Geostandards and Geoanalytical Research* 29, 333-338. https://doi.org/10.1111/j.1751-908X.2005.tb00904.x

Kimura, J.-I., Chang, Q., Ishikawa, T., Tsujimori, T. (2016) Influence of laser parameters on isotope fractionation and optimisation of lithium and boron isotope ratio measurements using laser ablation-multiple Faraday collector-inductively coupled plasma mass spectrometry. *Journal of Analytical Atomic Spectrometry* 31, 2305–2320. https://doi.org/10.1039/C6JA00283H

Marschall, H.R., Wanless, V.D., Shimizu, N., Pogge von Strandmann, P.A.E., Elliott, T., Monteleone, B.D. (2017) The boron and lithium isotopic composition of mid-ocean ridge basalts and the mantle. *Geochimica et Cosmochimica* Acta 207, 102–138. https://doi.org/10.1016/j.gca.2017.03.028

Martin, C., Flores, K.E., Harlow, G.E. (2016) Boron isotopic discrimination for subduction-related serpentinites. *Geology* 44, 899-902 https://doi.org/10.1130/G38102.1

Martin, C., Flores, K.E., Vitale-Brovarone, A., Angiboust, S., Harlow, G.E. (2020) Deep mantle serpentinization in subduction

zones: Insight from in situ B isotopes in slab and mantle wedge serpentinites. *Chemical Geology* 545, 119637. https://doi.org/10.1016/j.chemgeo.2020.119637

Paris, G., Gaillardet, J., Louvat, P. (2010) Geological evolution of seawater boron isotopic composition recorded in evaporites. *Geology* 38, 1035–1038. https://doi.org/10.1130/G31321.1

Rose-Koga, E.F., Sheppard, S.M.F., Chaussidon, M., Carignan, J. (2006) Boron isotopic composition of atmospheric precipitations and liquid–vapour fractionations. *Geochimica et Cosmochimica Acta* 70, 1603–1615. https://doi.org/10.1016/j.gca.2006.01.003

Scambelluri, M., Tonarini, S. (2012) Boron isotope evidence for shallow fluid transfer across subduction zones by serpentinized mantle. *Geology* 40, 907–910. https://doi.org/10.1130/G33233.1

Spivack, A.J., Edmond, J.M. (1987) Boron isotope exchange between seawater and the oceanic crust. *Geochimica et Cosmochimica Acta* 51, 1033–1043. https://doi.org/10.1016/0016-7037(87)90198-0

Standish, C.D., Chalk, T.B., Babila, T.L., Milton, J.A., Palmer, M.R., Foster, G.L. (2019) The effect of matrix interferences on *in situ* boron isotope analysis by laser ablation multi-collector inductively coupled plasma mass spectrometry. *Rapid Communications in Mass Spectrometry* 33, 959–968. https://doi.org/10.1002/rcm.8432

Vils, F., Tonarini, S., Kalt, A., Seitz, H.-M. (2009) Boron, lithium and strontium isotopes as tracers of seawater–serpentinite interaction at Mid-Atlantic ridge, ODP Leg 209. *Earth and Planetary Science Letters* 286, 414–425. https://doi.org/10.1016/j.epsl.2009.07.005

Yamada, C., Tsujimori, T., Chang, Q., Kimura, J.I. (2019) Boron isotope variations of Franciscan serpentinites, northern California. *Lithos* 334–335, 180–189. https://doi.org/10.1016/j.lithos.2019.02.004